

Fig. 1: Geometry of Line A (a); Line B (b); Line C(c).

The measurement data used in the present study comprise all of the measured vibration events that involve wind data from December 2008 to July 2009. It should be noted that the wireless sensor that was developed by TEPCO to measure the vibration acceleration of the conductor bundle in the three directions, was mounted on the spacer frame of the conductor bundle. The wind and acceleration measurements were synchronised for real time, but different sampling frequencies and/or different trigger levels were used for each type of data. The wind velocity data were recorded continuously for four months. Therefore, 10-minute-length wind records that correspond to each 10-minute-length acceleration data can be extracted appropriately from the continuous wind velocity data, in which a 10-minute-length wind record is commonly assumed to be stationary in practice. The summary of the field measurements is given in Table 1, and it indicates the number of datasets of all of the measured vibration events and the vibration events that have wind data.

Table 1 Number of field data sets (2008 – 2009).

Lines	Left Span		Jumper	Right Span	
	L/2	3L/4		L/4	L/2
Line A	-	-	-	44	191
Line B	104	220	121	137	157
Line C	10	61	-	52	1

3. FIELD DATA ANALYSIS

To have insight into the characteristics of gusty wind and dynamic responses in the field, the mean wind direction, mean wind velocity, wind turbulence intensity, RMS and MPPA of the dynamic displacement responses were first studied. It is noted that the measured acceleration is numerically integrated twice to obtain the time series for the displacement. Before each integration

step in the acceleration record, the data are filtered to remove the low-frequency components of noise by using the Butterworth high-pass filter with an appropriately selected cut-off frequency.

2.1 Wind-velocity data analysis

Figure 2 shows the variation in the direction and magnitude of the mean wind velocity during the measured vibrations along with the alignment of the transmission lines. The magnitude of the turbulence intensity is plotted with respect to the normal component of the mean wind velocity in Fig. 3. As seen in the figure, the direction of mean wind velocity is not normal to the transmission line and the variation in wind direction is large especially in the case of Line B. These turbulence intensities as supposed to be higher than normal.

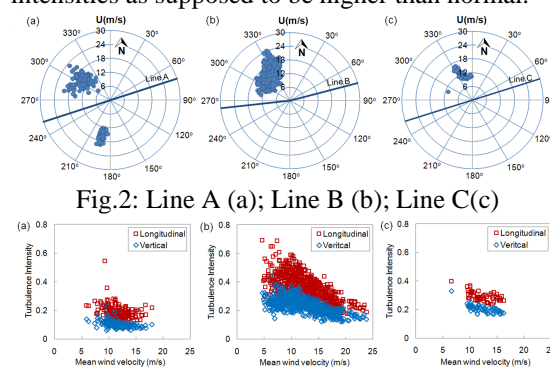


Fig. 3: Line A (a); Line B (b); Line C(c)

2.2 Vibration data analysis

Spectral analysis is conducted to investigate the time average characteristics of wind-induced responses in frequency domain as well as to obtain RMS of response and compare with eigenvalue analysis. In the following, for example, PSD of all measured points of the three transmission lines are shown. PSDs of selected data are shown in Fig. 4. For example, in the case of Line A, at mid-point measurement, there is some dominant peak of frequency at 0.1 Hz in horizontal spectra, 0.2 Hz in vertical spectra, and 0.3Hz in torsional spectrum. These peak response will be discussed later.

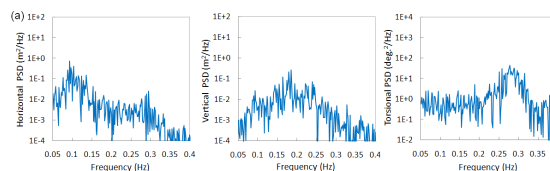


Fig. 4: PSDs of large amplitude vibrations in Line A at L/2 span.

The RMS of the horizontal, vertical, and torsional responses in Line A, Line B, and Line C are plotted with respect to the normal component of the mean wind velocity. For example, Fig. 5 shows RMS of Line B. It is noted that the RMS responses appeared to be more correlative with the normal wind component than the mean wind component.

As shown in Fig. 5, the trend of the RMS response versus the normal component of the wind is parabolic in almost all of the cases, except for the vertical vibration of Line C (Hung et al. 2014).

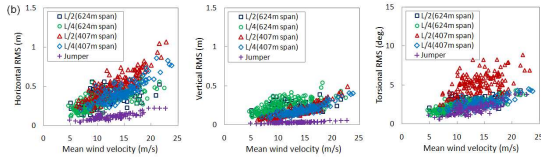


Fig.5. RMS response versus the normal component of the mean wind velocity of Line B

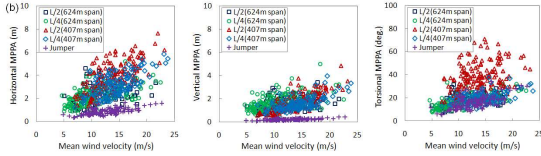


Fig.6. MPPA response versus the normal component of the mean wind velocity for Line B

Figure 6 shows the variation in the MPPA with respect to the normal component of the wind velocity for Line B, which is an example, that has the largest MPPA among the three transmission lines. The parabolic trend of MPPA in the figure is almost similar to the trend of the RMS response, which is also one of the characteristics of the gust response because the peak response can be obtained by multiplying the RMS response by a peak factor. While the RMS responses are relatively small for Line A and Line C (Hung et al. 2014), there is an event that shows very large responses with horizontal, vertical, and torsional MPPAs of 7.65 m, 4.83 m and 71.0 degree, respectively, at the middle point of the 407 m span of Line B. This type of event should be carefully identified as a gust response or a galloping phenomenon in further analysis.

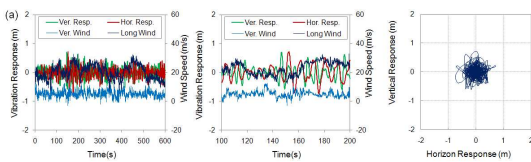


Fig. 7: Time series of Line A at L/2.

In order to understand further the nature behavior of large vibrations discussed, it is necessary to show time series of these vibrations and compared them with corresponding time series of wind velocity. In case of galloping, responses develop gradually due to negative aerodynamic damping. Opposite is the case of gust response in which response builds suddenly within very short time period and do not have gradually building cycles before appearance of peak cycle. Almost horizontal, vertical, and torsional responses appear suddenly and are not gradually developed

Moreover every sudden peak is accompanied by a sudden change in wind velocity. Impulsive nature of these peaks indicates the possibility that observed vibrations are gust response. The time history of typical events in Fig. 7 again confirm that, different from galloping response, the LAGs appear with the peak responses increasing suddenly within very short period of time corresponding to the increases of wind velocities.

4. CHARACTERIZATION OF RESPONSES WITH EIGENVALUE ANALYSIS

In order to evaluate the dynamic characteristics of the transmission line systems and identify the modal parameters from the field-measured data, the eigenvalue analysis is performed. The results of eigenvalue analysis, in which the proper FE models of the transmission lines with their accurate static-equilibrium-configurations play an important role not only are used to interpret the field-observed vibrations but also are used in a conjunction with the wind-force model to conduct the gust response analysis. The FE models of the transmission lines are created and analyzed by using the general-purpose computing program FEMAP/NX Nastran.

4.1. Finite element model of the transmission line system

In creating the FE models of the transmission lines, the important part is to find out the appropriate static equilibrium configurations of the conductors subjected to the body loads. Catenary theory is popular solution for static equilibrium configuration of cable under its self-weight. Catenary equation can be obtained based on assumption of extensible or inextensible cable. Based on theory of inextensible or extensible catenary, the static equilibrium configuration of conductor in FE model of the transmission line system in FEMAP/NX Nastran computing software is derived and presented. The equation of inextensible catenary curve can be given as follows.

$$z = \frac{H}{q_0} \cosh\left(\frac{q_0}{H}x + C_1\right) + C_2 \quad (1)$$

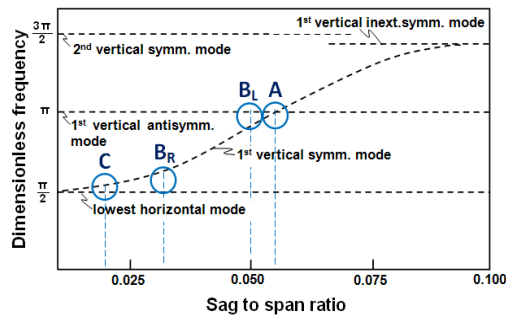
The equation of extensible catenary curve in z coordinate and x coordinate can be shown in Eq. (2) and Eq. (3), respectively, as follows.

$$z = \frac{I}{AE} \left(\frac{q_0 s_0^2}{2} - F s_0 \right) + \frac{1}{q_0} \sqrt{H^2 + (q_0 s_0 - F_3)^2} + C \quad (2)$$

$$x = \frac{H}{AE} s_0 + \frac{HL_0}{w} \cosh\left(\frac{q_0 s_0 - F_3}{H}\right) + C \quad (3)$$

where s_0 is un-deformed length (s = Lagrangian coordinate); q_0 is conductor weight per unit

length; AE is axial stiffness of conductor; x and z are Cartesian coordinates; H is the constant horizontal component of cable tension.



Note: A: Line A; B_L, B_R: Left and right span of Line B, respectively; C: Mid-span of Line C.

Fig. 8: Change in natural frequencies with respect to sag-to-span ratio and the position of Line A, B and C.

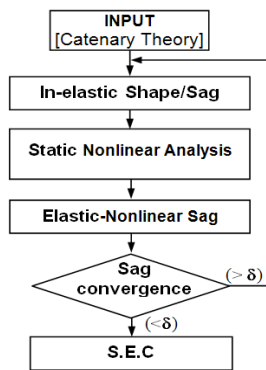


Fig. 9: Scheme of the iterative algorithm

The sags in the FE models should be set equal to the field-measured sags of real conductors, because the sag-to-span ratio affects significantly on the natural frequencies of vertical symmetric modes as shown in Fig. 8 (Irvine, 1981). Therefore, in order to derive the target conductor configuration of FE model, an alternative program will be proposed. In the procedure of deriving the target cable configuration of FE model, the “real coordinate data” is just considered as input coordinate data of initial configuration in beginning step of the alternative program. The initial configuration of cable can be arbitrary. Therefore, in the beginning step of the alternative program, it should freely select “the real coordinate data” to be the initial configuration. Therefore, “the real coordinate data” or the catenary theory calculated coordinate is considered as input coordinate data, not directly used as the FE target conductor configuration. The static equilibrium configuration analysis associated with pre-stiffening of the transmission lines under their body loads for inducing the tension inside the conductors is a nonlinear problem, which is solved by an iterative algorithm employing the sag as a convergence controlled parameter as shown in Fig. 9.

The details of FE models for different components in three transmission lines are indicated in Fig.10. The modeling of electric conductors is most essential in the FE modeling of the transmission line systems. FEMAP with NX Nastran is different from other commercial software. It does not deal with cable element. For modeling cable property, tension-only one-dimension element has been used.

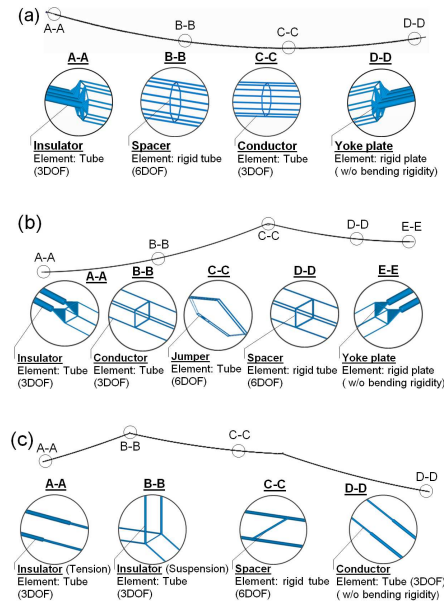


Fig.10: FE models of the transmission lines: (a) Line A; (b) Line B; and (c) Line C.

4.2. Eigenvalue analysis

The eigenvalue analyses are then conducted for the FE models of the transmission lines with proper static equilibrium configurations, and the results of eigenvalue analyses are summarized in Table 2.

In the case of Line B, Figure 11 shows a coupling of jumper vibration with two-loop torsional mode of 407 m span in Line B. The corresponding natural frequency is 0.34 Hz. The figure shows clearly the coupling of horizontal and torsional vibrations of jumper with the torsional mode of the shorter span. Such coupling mode is important in the sense that large vibration in the jumper can be induced by wind-induced span-vibration and result in its damage as observed by TEPCO.

Table 2 Natural frequencies and mode shapes of the transmission lines.

Line	Horizontal	Vertical	Torsion
Line A	0.096 Hz	0.180 Hz	0.148 Hz
	0.192 Hz	0.190 Hz	0.201 Hz
	0.287 Hz	0.293 Hz	0.298 Hz
	0.383 Hz	0.382 Hz	0.394 Hz
Line B	0.099 Hz	0.145 Hz	0.131 Hz
	0.156 Hz	0.190 Hz	0.183 Hz
	0.197 Hz	0.195 Hz	0.212 Hz
	0.296 Hz	0.298 Hz	0.313 Hz
	0.310 Hz	0.312 Hz	0.337 Hz
Line C	0.168 Hz	0.177 Hz	0.181 Hz
	0.178 Hz	0.186 Hz	0.189 Hz
	0.300 Hz	0.309 Hz	0.312 Hz
	0.337 Hz	0.344 Hz	0.348 Hz
	0.357 Hz	0.359 Hz	0.364 Hz

The spectral analysis is first conducted to investigate the time-averaged characteristics of wind-induced responses and wind velocities in the frequency domain. The dominant frequencies are then identified based on the peak response spectrum with the analytical natural frequencies and mode shapes. Example of PSD of field-measured, wind-induced responses in the Line A are depicted in Fig. 12. All the dominant peak frequencies in the PSD are very close to the analytical natural frequencies, as shown in the figure where the analytical natural frequencies and associated mode shapes are also indicated. In the case of Line A, there exist two equal-level dominant peaks corresponding to one-loop and two-loop modes in the horizontal PSD of quarter span response.

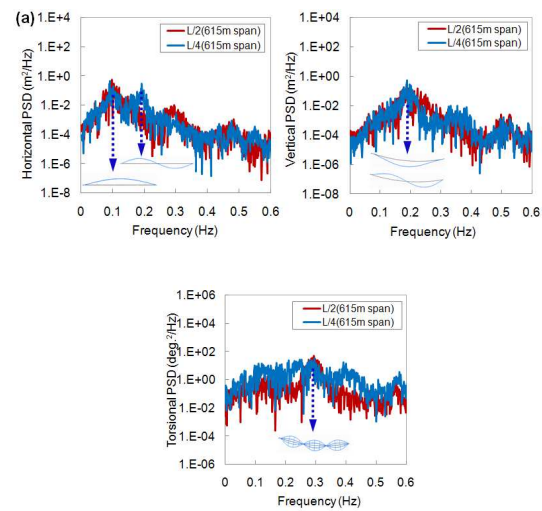


Fig.12: Examples of PSD of field measured responses of Line A.

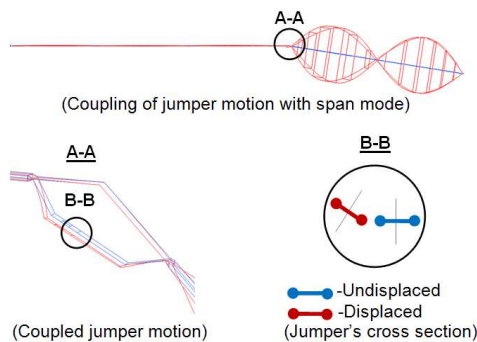


Fig.11: Coupling of jumper motion with two-loop torsional mode of 407 m span in Line B.

4.3. Interpretation of characteristics of field-measured vibration

The characteristics of field measured vibrations can be understood by the analytically evaluated natural frequencies and mode shapes.

5. INTERPRETATION OF FIELD-MEASURED RESPONSES BASED ON GUST RESPONSE ANALYSIS

The framework of the buffeting theory that was proposed by Davenport 1962 is popular for the gust-response prediction of the civil structures such as bridges, towers and the transmission line in the frequency domain, in which the spectral analysis and statistical computation that is associated the modal-based structural analysis are the core. The theory also introduces a so-called correction functions such as the aerodynamic admittance function, coherence function to deal with assumptions of the quasi-steady theory. Even though the theory needs to accept the existence of the assumptions and uncertainties, but Davenport's method validates for the gust response prediction of the line-like structure in practice.

Davenport's approach for determining the resonant dynamic responses of a structure in the particular modes under gusty wind is summarized in Fig. 13 and is applied to analyze the wind-induced vibrations of the transmission lines.

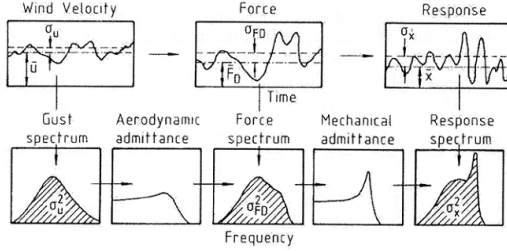


Fig. 13: Davenport's approach for wind-induced resonant response (Davenport 1967)

In the frequency domain, the buffeting theory presented in Fig. 13 can be expressed by Eq. (4). Equation (4) is derived by neglecting both the aerodynamic interaction among conductors in a conductor bundle and nearly-zero lift force in individual conductor because of circle-cross section of conductor. The first assumption is plausible because the separation between two conductors is larger than 10 times of conductor diameter (Zhang et al., 2000) and the second assumption can be justified by conductor's circular shape in absence of ice. Buffeting theory is presented in detail in Appendix B.

$$S_r(f) = S_u(f) \times [\rho C_D \chi(f_i) d_c n_c l \bar{U}]^2 \sum_{i=1}^N \frac{\phi_i^2}{M_i^2} |J(f_i)|^2 |H(f_i)|^2 \quad (4)$$

where S_r , S_u are the power spectral densities of dynamic response and wind velocity fluctuation, ρ is the air density, C_D is the drag force coefficient for a single conductor, $|\chi_i(f)|^2$ is the aerodynamic admittance, d_c is the diameter of conductor, n_c is the number of conductors in a bundle, l is the span of the transmission line, \bar{U} is the mean wind velocity normal to the transmission line, ϕ_i is the mode shape vector of i^{th} mode. M_i is the mass-normalized coefficient.

The measured wind data is used to calculate the gust responses of three transmission lines, while there are many uncertain parameters assumed in the gust response analysis. Table 3 and 4 summarized the assumed values of that uncertain variable in the present analysis

Table 3 Uncertain parameters assumed in gust response analysis.

Variable	Description	Value
ρ	Air density (kg/m^3)	1.204
$C_{D,L,M}$	Drag coefficient single conductor	1.0
χ	Aerodynamic admittance	1
k	Empirical constant in frequency dependant correlation of wind velocity	15

Table 4 Aerodynamic damping ratios assumed in gust response analysis.

Mode	Line A			Line B			Line C		
	Hor.	Vert.	Tor.	Hor.	Vert.	Tor.	Hor.	Vert.	Tor.
1	6%	4%	2%	5%	2%	2%	4%	2%	1%
2	7%	3%	2%	4%	2%	1%	3%	3%	1%
3	5%	3%	1%	4%	2%	1%			
4	4%	3%	1%						

The analytically evaluated RMS responses were compared with all the measured-vibration data at all the measure point of three transmission lines, and it was found that almost all the cases show good agreement. In the followings, therefore, some important examples of RMS comparison are only discussed. In order to understand completely the field-measured vibrations, beside the cases of good agreement in RMS comparison, some other cases with the particular characteristics are also selected to be discussed.

One example of the good agreement in the horizontal RMS comparisons is the case of Line A at the mid-point of 615 m span, as shown in Fig. 14 (a). It is found that all of three response components are reproduced very well by the theory-based gust response analysis. The good-agreement can be understood by looking into the PSD comparison of each event, and the PSD of typical event in the gust response analysis of Line A is depicted in Fig. 14 (b), in which the analytical and experimental responses show very small discrepancy.

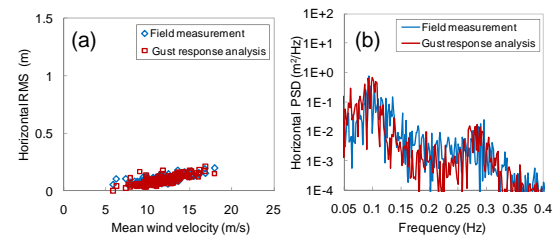


Fig. 14: Horizontal RMS (a) and one event of Horizontal PSD comparison (b) at L/2 of 615 m span in Line A.

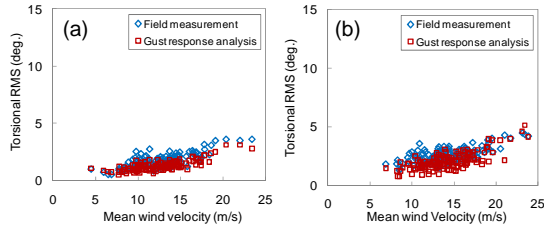


Fig. 15: RMS comparison of coupled jumper and span responses in Line B: (a) Torsional RMS of jumper; (b) Torsional RMS of L/4-407 m span.

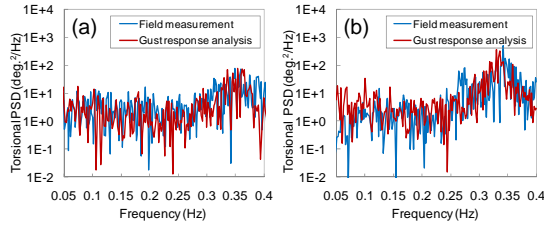


Fig. 16: PSD Comparison of jumper in Line B. (a) Torsional PSD of jumper and (b) Torsional PSD of quarter-point 407 m span.

As mentioned previously in the results of eigenvalue analysis, the horizontal and torsional motions of jumper are coupled with the torsional motion of span at the natural frequency of 0.34 Hz in the case of Line B. This characteristic was reflected in the gust response analysis and results in the good agreement in the RMS comparison in Fig. 15, which is supported by the small discrepancy in PSD comparison in Fig.16. The coupling characteristics can be also seen in these figures. The torsional RMS responses of jumper in Figs. 15(a) show similar tendency to the torsional RMS response of the quarter-point of 407 m span in Fig. 15(b), and all of the PSD comparisons in Fig. 16 show the same dominant peaks around their coupling frequency of 0.34 Hz.

6. PREDICTION OF LARGE AMPLITUDE GUST RESPONSE IN TIME DOMAIN

A significant feature of approach of time-domain gust response analysis is that the time-dependent characteristics of the unsteady aerodynamic forces and nonlinearities of the both aerodynamic and structural origins can be taken into account. In this analysis, the direct response analysis method is employed. The direct method that performs numerically the time integration on the complete coupled equations of motion is applied in this analysis.

6.1. Equation of motion

Multi-DOF motion equations of the transmission line conductor subjected to the buffeting forces is expressed generally as follows:

$$\mathbf{M}\ddot{\mathbf{u}}(x,t) + \mathbf{C}\dot{\mathbf{u}}(x,t) + \mathbf{K}\mathbf{u}(x,t) = \mathbf{F}_b(t) \quad (5)$$

where $\mathbf{u}(x,t)$, $\dot{\mathbf{u}}(x,t)$, $\ddot{\mathbf{u}}(x,t)$ are the deflection and its first, second order derivatives. \mathbf{M} , \mathbf{C} , \mathbf{K} are the mass, damping, stiffness matrices; $\mathbf{F}_b(t)$ is the buffeting forces.

The buffeting forces per unit length of conductor bundle can be expressed and corrected by the frequency-dependant admittance functions as follows.

$$L_b(t) = \frac{1}{2} \rho U^2 d_c n_c \left[C_L \chi_{L_u}(f) \frac{2u(t)}{U} + (C'_L + C_D) \chi_{L_w}(f) \frac{w(t)}{U} \right] \quad (6.a)$$

$$D_b(t) = \frac{1}{2} \rho U^2 d_c n_c \left[C_D \chi_{D_u}(f) \frac{2u(t)}{U} + (C'_D - C_L) \chi_{D_w}(f) \frac{w(t)}{U} \right] \quad (6.b)$$

$$M_b(t) = \frac{1}{2} \rho U^2 (d_c n_c)^2 \left[C_M \chi_{M_u}(f) \frac{2u(t)}{U} + C'_M \chi_{M_w}(f) \frac{w(t)}{U} \right] \quad (6.c)$$

where C_L , C_D , C_M are the aerodynamic coefficients at the balanced angle; C'_L , C'_D , C'_M are the first-order derivatives with respect to the angle of attack; d_c, n_c are the diameter of the bundle-conductor and number of bundled-conductor; $\chi_{F_v}(F=L, D, M; v=u, w)$ is the aerodynamic transfer functions between the turbulent components and forces.

Based on the dynamic equation of the motion in the matrix form as shown in Eq.(5), the structural response is solved at each fixed discrete-time step Δt .

6.2. Wind-field simulation

It is difficult to obtain the time series of wind velocity at all points in the site. Therefore, the digital simulation techniques are often used to generate the time series of wind field at all of the simulated nodes. In the time domain analysis, the accurate of results depends significantly on the simulated time series of wind load acted on the conductors since the aerodynamic response are sensitive to the winds (Chen et al., 2000). Nodal-wind force per unit length of conductor is calculated using Eq. (6) based on the mean wind velocity and the turbulent wind that vary in the time and space along span.

There are some wind-field-simulation techniques to simulate the stochastic wind field, in which spectral representation technique and time-series representation one are often used. The present analysis employs the spectral representation

technique to generate the nodal wind time-series based on the measured wind records.

The transmission line conductor is a two-dimensional, large-scale structure. The continuous wind fields should be divided into the finite parts to facilitate the calculation. Each part has two components; mean and turbulent wind in three directions, along $u(t)$, vertical $v(t)$, and lateral $w(t)$ turbulences (Simiu and Scanlan, 1978). Because of the small effect, the longitudinal turbulent wind $w(t)$ is often neglected. Along and vertical turbulent components $u(t)$, $w(t)$ are considered as two multi-variate spatially-correlated Gaussian-random processes with zero mean. The turbulent fields at “ n ” discrete nodes (Fig.17) are expressed as follows:

$$u(t) = \{u_1(t), u_2(t), \dots, u_n(t)\}^T \quad (7.a)$$

$$v(t) = \{v_1(t), v_2(t), \dots, v_n(t)\}^T \quad (7.b)$$

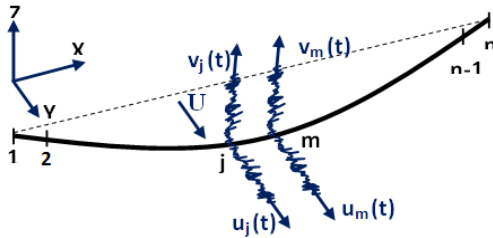


Fig.17: Turbulent field at nodes.

To simulate spatial wind, the cross-spectral density matrix $S^0(\omega)$ of one-dimension n -variate process $[u(t) \text{ or } w(t)]$ is constructed as follows:

$$S^0(\omega) = \begin{bmatrix} S_{11}^0(\omega) & S_{12}^0(\omega) & K & S_{1n}^0(\omega) \\ S_{21}^0(\omega) & S_{22}^0(\omega) & K & S_{2n}^0(\omega) \\ M & M & M & \\ S_{n1}^0(\omega) & S_{n2}^0(\omega) & K & S_{nn}^0(\omega) \end{bmatrix} \quad (8)$$

To simulate the one-dimensional multi-variate stationary stochastic process, using Cholesky's method, $S^0(\omega)$ can be performed as follows in which $H(\omega)$ matrix is a lower-triangular matrix:

$$S^0(\omega) = H(\omega)H^{T*}(\omega) \quad (9)$$

$$H(\omega) = \begin{bmatrix} H_{11}(\omega) & 0 & K & 0 \\ H_{21}(\omega) & H_{22}(\omega) & K & 0 \\ M & M & M & \\ H_{n1}(\omega) & H_{n2}(\omega) & K & H_{nn}(\omega) \end{bmatrix} \quad (10)$$

Then, the stochastic process can be simulated by the following series (Wag et al.)

$$f_j(t) = 2 \sum_{m=1}^j \sum_{l=1}^N |H_{jm}(\omega)| \sqrt{\Delta\omega} \cos(\omega_{ml}t - \theta_{jm}(\omega_{ml}) + \phi_{ml}) \quad (11)$$

Where $f(t) = u(t), w(t)$; $j = 1, 2, \dots, n$; m is moving node index; l is moving point/freq. range; N is frequency interval number; Δn is frequency interval; n_{ml} is frequency point/freq. range; θ_{ji} is complex phase angle of H_{jm} ; ϕ_{ml} is random phase angle $[0-2\pi]$.

In the application, a grid of the structural coordinate has the height and width of 100m and 600m, respectively, in which the number of horizontal segment and vertical segment are 30 and 10 segments, respectively. The mean-wind velocity at the referred point is 19.4m/s (top of tower). The fitting result of the referred-point spectra to Kaimal spectra model $\frac{fS_u(f)}{u_*^2} = \frac{an}{(1+bn)^{5c/3}}$ that is used to

simulate the grid-point turbulence spectra is conducted as follows: $a=220$; $b=45$; $c=0.95$ with $k=0.4$; $z1=0.01m$; $z2=100m$; $u_* = 1.5$; $\alpha=0.2$ (terrain condition) whereas in the Kaimal spectrum the parameters are $a=200$; $b=50$; $c=1$. The along-turbulence spectra comparisons are plotted in Fig. 18.

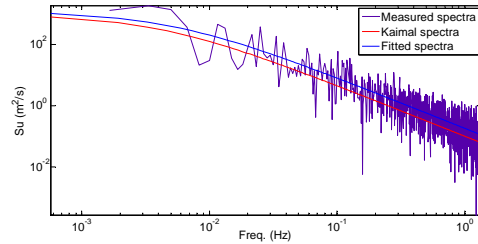


Fig.18: Comparison of PSD in along wind direction.

Results of the simulated-wind time series of Line A listed as follows. In the Fig.19, the distribution of the wind series along span (same elevation) is considered at mid- and quarter-span, for example. Figure 20 shows two nodal-wind time series at two sample grid points. It could be said that it is impossible to obtain the simulated-wind field that is equal exactly to the measured-wind field because of the stochastic procedure. However, with the consideration of the fitting the spectra model to the measured spectra and the terrain condition in the site, the result of the wind simulation is expected to be appropriate with the wind field.

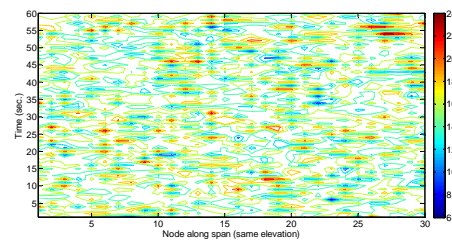


Fig.19: Distribution of the wind series along span at L/2 span.

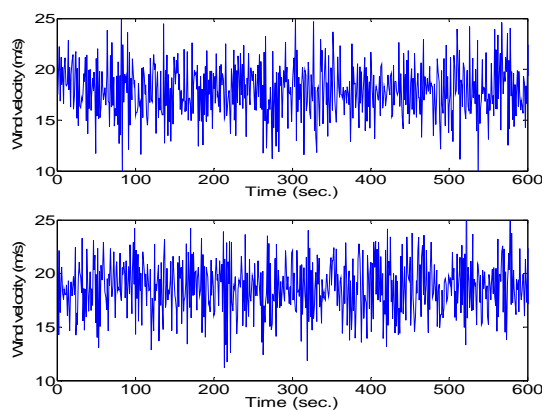


Fig.20: Wind time series at node

6.3. Gust response simulation

The time-domain gust-response analysis of Line A (Fig.21) subjected to the simulated-wind is conducted by using the basic NX Nastran solver. The time series of drag-, lift- and torsional-wind forces are calculated by using Eq.6. Based on length of elements, the nodal-wind-force time series is obtained. For example, the nodal-wind-force time series at mid-span that is resulted from assumed parameters in Table 5 is shown in Fig.22.

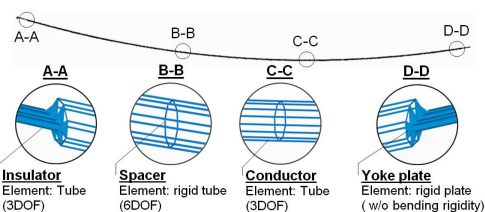


Fig.21: FE model of Line A

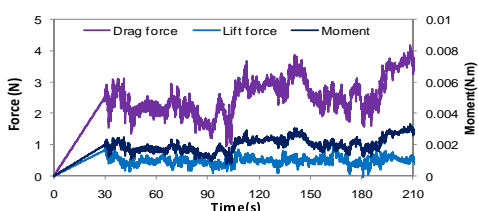


Fig. 22. An example of nodal wind force of sub-conductor at mid-span with 30s-gredually-increased loading

Table 5

ρ (kg/m ³)	U(m/s)	d_c (m)	n_c	χ	C_D	C'_D
1.204	17.9	0.0403	8	1	0.76;	0.1; -
					0.05;	0.006; -
					-0.003	0.0002

The basic NX Nastran solver is employed to analyze the time-domain-gust response, in which the solver is setup to run a 26000-step calculation

with 0.02-second of the time increment to obtain a 200-second vibration-response time series. Damping ratio is selected to be 1% critical damping that is recommended for dynamic analysis in NX Nastran.

Figure 23 (a), (b), and (c) show the time series of the conductor-response at mid-span in the horizontal, vertical, and torsional directions, respectively. In case of horizontal response, amplitude of vibration response is larger than field-measured response. This could be due large along wind force even a pre-loading of 30 seconds was applied. From 100th second to 200th second, the vibration amplitude of both simulation and measurement has good agreement about response magnitude and shape of response. As mentioned previously, the second half of response history, conductor vibrated without affection of along wind force at beginning of loading.

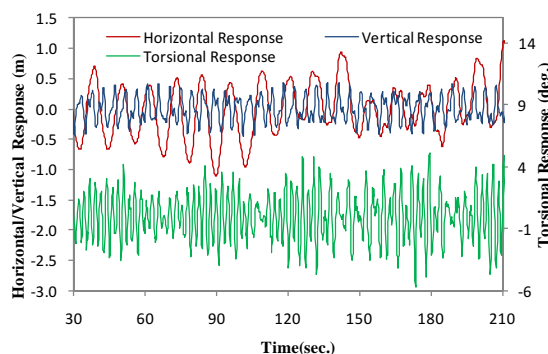


Fig. 23: Time series of response at mid-span.

7. CONCLUSIONS

The full-scale measurements of the large-amplitude vibrations and their characterization by the extensive analysis of the enormous numbers of datasets are conducted in the different types of the transmission lines. The essential conclusions can be summarized as follows.

The field-measurements of wind-induced vibration and wind-field data in the three different types of the transmission lines enable the interpretation of the field-observed vibrations. The high turbulence intensities and the parabolic pattern of RMS response verses the mean wind velocity indicate the possibility of the observed vibrations as gust responses. Based on scattering of RMS response, the larger conductor bundle seems to be more stable than the other ones.

The results of eigenvalue and gust-response analyses give meaningful information in the identification of the field-measured events, in which the proper FE models of the transmission

lines with their accurate static-equilibrium-configurations play an important role. A coupling between the similar-length spans pointed out that the span length affects significantly to the natural frequencies and mode shapes. In the conductor bundle, the type of spacer does not change much their torsional frequencies and model shapes.

The reasonable agreement of RMS between the gust-theory and the field responses as well as their PSDs confirms that most of the observed vibrations could be the gust response. The Buffeting theory is usable to different type of the bundled-conductor transmission lines. There might be a possibility of galloping phenomena in some cases and more vivid interpretation for identifying the galloping phenomenon is required in future.

For further interpretation about the large-amplitude gust response developed in time, the time-domain-gust analysis is considered. The significant feature of this approach is that the time-dependent characteristics of the unsteady-aerodynamic forces and nonlinearities of the both aerodynamic and structural origins can be taken into account in estimating the gust response. In future works, the results is expected to be improved for the design code or usable for controlling the large-amplitude vibration in order to avoid the phase-to-phase flashover that could lead to interrupt the electrical-power supply.

Based on the long-time observation at the site by TEPCO in the different type of the transmission line systems, the present analysis is a first extensive and intensive study on the causes of the recently field observed damages in the very long-span, large bundled-conductor transmission line systems. The most meaningful point of the researches is to confirm that the large-amplitude field-measured vibration is gust response. The gust responses can be sufficient large to cause the damages in the overhead transmission lines. The confirmation blasts the embroilments in the identification of vibration characteristics. The results may be a good reference for the design-code evaluation as well as the application of the vibration control to minimize the large-amplitude vibration.

REFERENCES

Blevins, R.D., Iwan, W., 1974. The galloping response of a two-degree-of-freedom system. *J. Appl. Mech.*, 41, 1113-1118.

CIGRÉ 2005. "State of the Art of Conductor Galloping, Technical Brochure No. 322" CIGRE TF B2.11.06.

Davenport, A.G., 1962. The response of slender, line-like structures to a gusty wind. *Proceeding of the ICE*, 23, 389-408.

[Den Hartog, J.P., 1932. Transmission Line Vibration due to sleet. *AIEE Trans.*, 51, 1074-1086.](#)

Desai, Y.M., Yu, P., Popplewell, N., Shah A.H., 1995. Finite element modelling of transmission line galloping. *Comput Struct.*, 57, 407-420.

[Diana, G., Cheli, F., Nicolini, P., Tavano F., 1990. Oscillation of bundle conductors in overhead lines due to turbulent wind. *IEEE Trans Power Delivery*, 5\(4\), 1910-1922.](#)

Fekr, M.R., McClure, G., 1998. Numerical modelling of the dynamic response of ice-shedding on electrical transmission lines. *Atmospheric Research* 46, 1-11.

[Gull, J.H., Yamaguchi, H., Kumagai, K., Hung, P.V., 2011. Interpretation of field-measured vibrations in transmission lines by gust response analysis. *Proceedings of 9th International Symposium on Cable Dynamics, Shanghai \(China\)*, 281-286.](#)

[Gurung, C.B., Yamaguchi H., Yukino T., 2003. Identification of large amplitude wind-induced vibration of ice-accreted transmission lines based on field observed data. *Journal of Wind Engineering and Industrial Aerodynamics*, 91\(7\), 903-924.](#)

[Havard, D.G., Pohlman J.C., 1979. Field-testing of detuning pendulums for controlling galloping of single and bundle conductors. Paper A79 499-5. *IEEE Symposium on Mechanical Oscillations of Overhead Transmission Lines. Vancouver, Canada, July.*](#)

Holme, J.D., 2001. *Wind loading of structures.* London Spon Press.

Hung et al., 2014. Large amplitude vibrations of long-span transmission lines with bundled conductors in gusty wind. *J. Wind Eng. Ind. Aerodyn.* 126, 48-59.

Hunt, J., Richards, D., 1969. Overhead line oscillations and the effect of aerodynamic damper. *Proc. IEEE*, London, 1869-1874.

Impollonia, N.; Ricciardi, G., Saitta, F., 2011. Vibrations of inclined cables under skew wind. *International Journal of Non-Linear Mechanics* 46, 907-918.

Irvine, H.M., 1981. *Cable structures.* The MIT Press.

Keutgen, R., Lilien, J.L., 2000. Benchmark cases for galloping with results obtained from wind tunnel facilities-validation of a finite element model. *IEEE Trans Power Delivery*, 15, 367-374.

Keutgen, R., Lilien, J.L., 1998. A new damper to solve galloping on bundle lines, theoretical background, laboratory and field results. *IEEE Trans.*, 13 (1), 260-265.

Keyhan, H., McClure, G., Habashi, W.G., 2013. Dynamic analysis of an overhead transmission line subject to gusty wind loading predicted by wind-conductor interaction. *Computers and Structures* 122, 135-144.

Matheson, M.J., Holmes, J.D., 1981. Simulation of the dynamic response of transmission lines in

strong winds. *Engineering Structures*, Vol.3, Issue 2, 105–110.

McClure, G., Lapointe, M., 2003. Modeling the structural dynamic response of overhead transmission lines. *Computers and Structures*, 81, 825–834.

Miguel, L.F.F, Riera, J.D., João Kaminski Jr., Menezes, R.C.R., 2012. Assessment of code recommendations through simulation of EPS wind loads along a segment of a transmission line. *Engineering Structures*, 43, 1–11.

Nakamura, Y., 1980. Galloping of bundled power line conductors. *J. Sound Vibr.*, 73, 363-377.

Nicholas, I., 2012. Davenport's mark on wind engineering. *J. Wind Eng. Ind. Aerodyn.*, 104-106.

Nigol, O., Buchan, P.G., 1981. Conductor galloping part I — Den Hartog mechanism. *IEEE Trans Power Apparatus Syst.*, 100(2), 699-707.

Nigol, O., Buchan, P.G., 1981. Conductor galloping part II — Torsional mechanism. *IEEE Trans Power Apparatus Syst.*, 100(2), 708-720.

Novak, M., Tanaka, H., 1974. Effect of turbulence on galloping instability. *J Eng. Mech.*, ASCE, 100, 27-47.

Ohkuma, T., Marukawa, H., 1999. Galloping of overhead transmission lines in gusty wind. *First International Conference on Advances in Structural Engineering and Mechanics*, Seoul (Korea), 71-76.

Ramberg, S.E., Griffin, O.M., 1977. "Free vibration of taut and slack marine cables." In: *Proceedings of the American Society of Civil Engineers*, Vol. 103, 2079-2092.

[Rawlins, C.B., 1981. Analysis of conductor galloping field observations — single conductors. IEEE Trans Power Apparatus Syst. 100\(8\), 80-89.](#)

[Richardson, A., 1965. Dynamic damper for galloping conductors. Elect. World, 154-155.](#)

[Stroman, E.N., 2006. Theory of Bridge Aerodynamics. Springer.](#)

[Wang, J., Lilien J.L., 1998. Overhead electrical transmission line galloping: A full multi-span 3-DOF model, some applications and design recommendations. IEEE Trans Power Delivery, 13\(3\), 909-916.](#)

Yamaguchi, H., Xie, X., Yukino, T., 1995. Galloping analysis of transmission lines with bundled conductors. *Proceeding of International Seminar on Cable Dynamics*, Liege (Belgium), 1995, 61–66.

[Yukino, T., Fujii, K., Hayase, I., 1995. Galloping phenomena of large bundled conductors observed on the full scale test line. Proceeding of International Seminar on Cable Dynamics, Belgium, 557-563.](#)

Zhang, Q., Popplewell, N., Shah, A.H., 2000. Galloping of bundle conductor. *Journal of sound and vibration* 234 (1), 115-134.